



**HAL**  
open science

## Genesis of Microstructures in Friction Stir Welding of Ti-6Al-4V

Gnofam Jacques Tchein, Dimitri Jacquin, Dominique Coupard, Eric Lacoste,  
Franck Girot Mata

► **To cite this version:**

Gnofam Jacques Tchein, Dimitri Jacquin, Dominique Coupard, Eric Lacoste, Franck Girot Mata. Genesis of Microstructures in Friction Stir Welding of Ti-6Al-4V. Metallurgical and Materials Transactions A, 2018, 49 (6), pp.2113-2123. hal-02353927

**HAL Id: hal-02353927**

**<https://hal.science/hal-02353927>**

Submitted on 7 Nov 2019

**HAL** is a multi-disciplinary open access archive for the deposit and dissemination of scientific research documents, whether they are published or not. The documents may come from teaching and research institutions in France or abroad, or from public or private research centers.

L'archive ouverte pluridisciplinaire **HAL**, est destinée au dépôt et à la diffusion de documents scientifiques de niveau recherche, publiés ou non, émanant des établissements d'enseignement et de recherche français ou étrangers, des laboratoires publics ou privés.



31  
32  
33  
34  
35  
36  
37  
38  
39  
40  
41  
42  
43  
44  
45  
46  
47  
48  
49  
50  
51  
52  
53  
54  
55  
56  
57  
58  
59  
60

**I. INTRODUCTION**

The Ti-6AL-4V alloy is widely used due to its good resistance to corrosion, high strength (even at high temperatures) and its biocompatibility. It has applications in several domains such as aeronautics, medical science and the automotive sector.

Due to titanium alloy’s good mechanical properties, such as its high melting point and high hardness, mastering the shaping processes of titanium alloys remains a challenging task, especially as welding titanium by conventional methods usually leads to a decrease in its mechanical properties [1]. To overcome these problems, Friction Stir Welding (FSW) could be used to maintain enhanced mechanical properties.

Friction Stir Welding is a solid-state welding process. Its main advantage is that it avoids most of the solidification defects usually encountered with other welding methods. This is why it is mainly performed on low melting point alloys such as aluminium [2–7] and magnesium [8–10]. FSW on titanium alloys is still rarely studied because it requires much more expensive experimental resources such as a cooling system or expensive welding tools [11–14]. Experimental research on FSW can be classified into two categories: optimisation/control of the process and effects of different FSW parameters on the microstructure.

Concerning optimisation/control of Ti-6Al-4V FSW, Edwards and Ramulu [13] studied the influence of two process parameters: rotational speed and welding speed. They were able to find adequate rotational and welding speeds for different plate thicknesses. The welding parameters were found to influence microstructure, penetration, void formation, and tool wear. Shojaeefard et al. [15] worked on Friction Stir Welds of AA1100. Microstructural and mechanical properties were optimised by the Design Of Experiments method (DOE). The welding parameters were rotational speed, shoulder diameter and welding speed, while the properties to optimise were ultimate tensile strength, grain size, and hardness. They simulated grain size evolution and validated it by experimental results. They found that welding speed played a major role in affecting grain size, hardness, and ultimate tensile strength (UTS) of the weld. Currently, much work is focused on FSW studies of dissimilar alloys [4–6,16,17]. In these cases, the material in the welded zone consists of a mixture of the two base materials and the weld’s mechanical properties are similar to those of the softer base material. Other studies are presently focused on tool wear mechanisms and tool materials used in FSW of Ti-6Al-4V [14,18,19]. W-Re, WC, p-CBN and W-La alloys are materials usually used for titanium alloys, but W-Re alloys are currently considered to be the most effective [14,20,21].

61 Regarding the effects of different FSW parameters on the material, Edwards and Ramulu [22] used  
62 thermocouples to determine the peak temperature in Ti-6Al-4V plates during FSW. By varying the welding and  
63 rotational speeds, temperatures were found to increase up to 1500K, leading to the conclusion that rotational  
64 speed has the dominant effect on the peak temperature and welding speed controls exposure time at peak  
65 temperatures. Zhang et al. [23] studied the microstructural and mechanical properties of Ti-6Al-4V weld joints  
66 for different welding and rotational speeds. They found that an increasing rotational speed led to decreasing  
67 hardnesses and tensile strengths. They observed a fully lamellar microstructure in the stirred zone and a duplex  
68 structure in the heat affected zone. Yoon et al. [24] studied the effect of tool rotational speed on microstructure  
69 and texture evolution during FSW of equiaxed Ti-6Al-4V plates. Inside the Stirred Zone a fully lamellar  
70 structure was observed near the top surface, while a fully equiaxed structure was found near the bottom surface  
71 of the weld. Esmaily et al. [25] studied the mechanisms of formation of the martensitic phase in Ti-6Al-4V FS  
72 welds. They welded several samples at different rotational speeds and constant welding speeds. They pointed out  
73 that a minimum rotational speed is necessary to obtain the martensitic phase in the stirred zone. Using this value,  
74 they obtained a bimodal structure.

75 The Ti-6Al-4V alloy is one of the most commonly used titanium alloy grades, and its mechanical properties can  
76 be easily modified by heat treatment. In this paper, we propose to study the influence of different pre-heat  
77 treatments on the genesis of microstructures in FSW of the Ti-6Al-4V alloy.

78

## 79 **II. EXPERIMENTAL PROCEDURES**

80

### 81 **A. Heat treatments**

82 Before welding, 5 mm thick commercial purity Ti-6Al-4V plates were heat treated. The chemical composition of  
83 this alloy is presented in Table 1. Table 2 shows the different pre-heat treatments performed before welding.  
84 Three of the most common heat treatments [26,27] were applied under argon shielding gas. These heat  
85 treatments result in a change in microstructure and mechanical properties (Figure 1).

86 The microstructure of the initial (without pre-heat treatment) material comes from a relatively complex thermo-  
87 mechanical treatment in the  $\alpha+\beta$  two-phase domain of the Ti-6Al-4V alloy. This treatment is used to break some  
88 of the  $\alpha_p$  (primary) laths already formed. The  $\alpha_p$  is formed during the solution heat-treatment in the  $\alpha+\beta$  domain.  
89 During the rolling of the sheets,  $\alpha_p$  debris can coalesce and recrystallize into small nodules which grow to  
90 become nodular primary  $\alpha$  grains ( $\alpha_{pn}$ ). The size of these grains depends on the temperature and the duration of

91 the heat treatment. These nodules can only be completely re-dissolved if the material is heated above  $\beta$ -transus  
92 temperature (995°C). The  $\beta_m$  and  $\beta_s$  phases are trapped outside the nodules to form a  $\beta$  matrix. The metastable  $\beta_m$   
93 phase corresponds to the non-equilibrium primary  $\beta$  phase, capable of being transformed and which can be  
94 maintained at ambient temperature by a local chemical composition which remains close to that of high  
95 temperatures. The stable  $\beta_s$  phase at room temperature is the primary  $\beta$  phase maintained at ambient temperature  
96 and stable due to a local concentration of  $\beta$ -stabiliser sufficient to maintain it, e.g. 15% of vanadium [28].

97 Both Figure 1.b and Figure 1.c show a primary lamellar  $\alpha$ -phase called the Widmanstätten phase. The shape of  
98 the laths depends on the duration of the heat treatments and the cooling rates: the slower the cooling, the larger  
99 the laths.

100 Figure 1.b (coarse lamellar) shows an intergranular Widmanstätten  $\alpha$ -phase ( $\alpha_{WI}$ ) surrounded by  $\beta$  and grain  
101 boundary Widmanstätten  $\alpha$ -phase ( $\alpha_{WGB}$ ). The latter germinates at the prior  $\beta$ -grain boundaries in a particular  
102 orientation with the  $\beta$  phase (Burgers relations). It grows towards the inside of the grain in the form of laths. The  
103 germination and growth of this phase is accompanied by a diffusion of (a)  $\alpha$ -stabiliser elements towards the  
104 laths, and (b)  $\beta$ -stabilisers outside these laths.

105 Figure 1.c (fine lamellar) shows only an intergranular Widmanstätten  $\alpha$ -phase surrounded by  $\beta$ . This phase  
106 germinates inside the ex- $\beta$  grains on sites such as dislocations or other defects. It is in the form of laths, either  
107 parallel (forming colonies of the same orientation), or entangled with two or three privileged orientations in the  
108 whole grain. These directions are often disoriented at 60°, corresponding to the angle between the 6  
109 transformation variants from  $\beta$  to  $\alpha$ . In this structure, intragranular  $\alpha$  is surrounded by  $\beta_m$  or  $\beta_s$  depending on the  
110 stability of the matrix.

111 Finally, an annealing heat treatment at the top of the  $\alpha + \beta$  domain was performed (Figure 1.d). This treatment  
112 stabilises the microstructure by dissolving the fine laths of  $\alpha$ . The  $\alpha$ -stabiliser alloying elements of this phase  
113 diffuse during the heat treatment and allow the growth of the nodular primary  $\alpha$  grains ( $\alpha_{pn}$ ). During cooling, the  
114  $\beta_m$  phase is transformed into  $\beta$  transformed ( $\beta_t$ ) grains and the intergranular  $\alpha$  -laths formed grow to varying  
115 degrees, depending on the cooling rate. This microstructure is called the duplex phase, and consists of equiaxed  
116 alpha grains (light) in a transformed beta matrix (dark) containing a coarse, acicular  $\alpha$  phase.

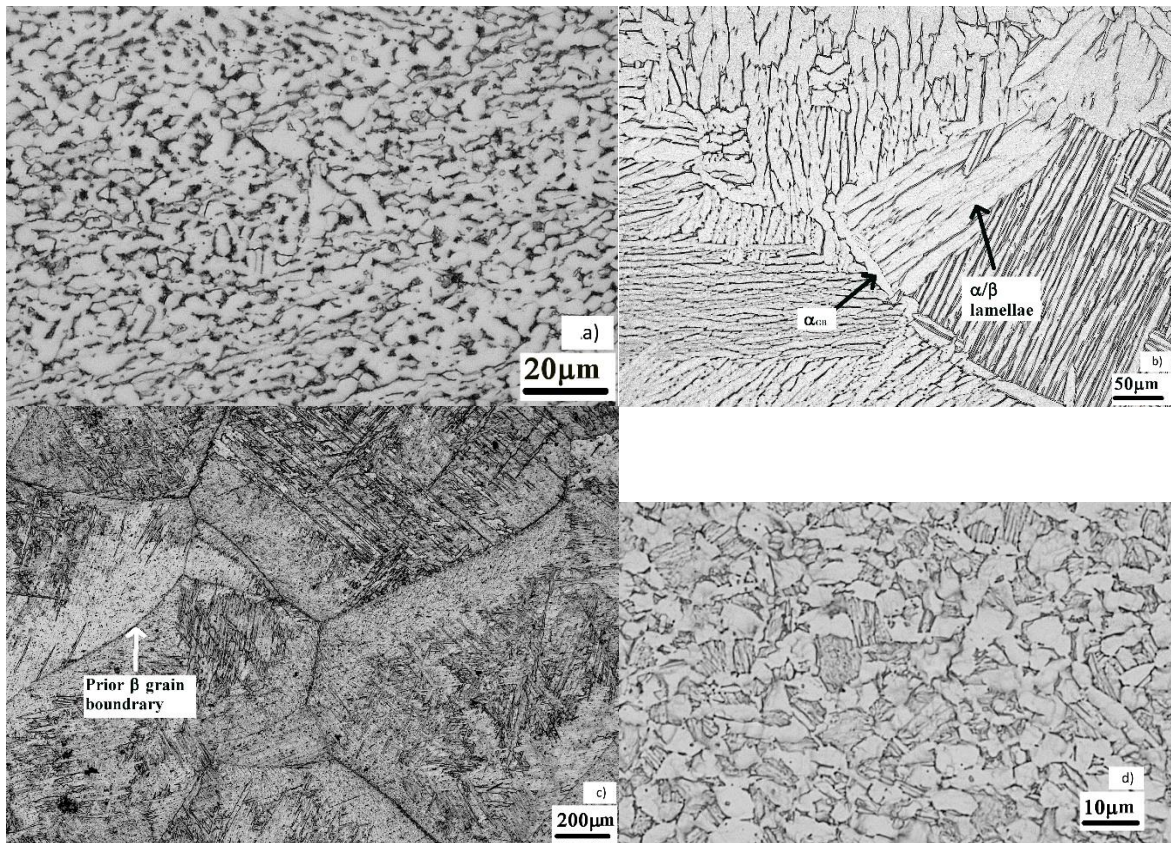


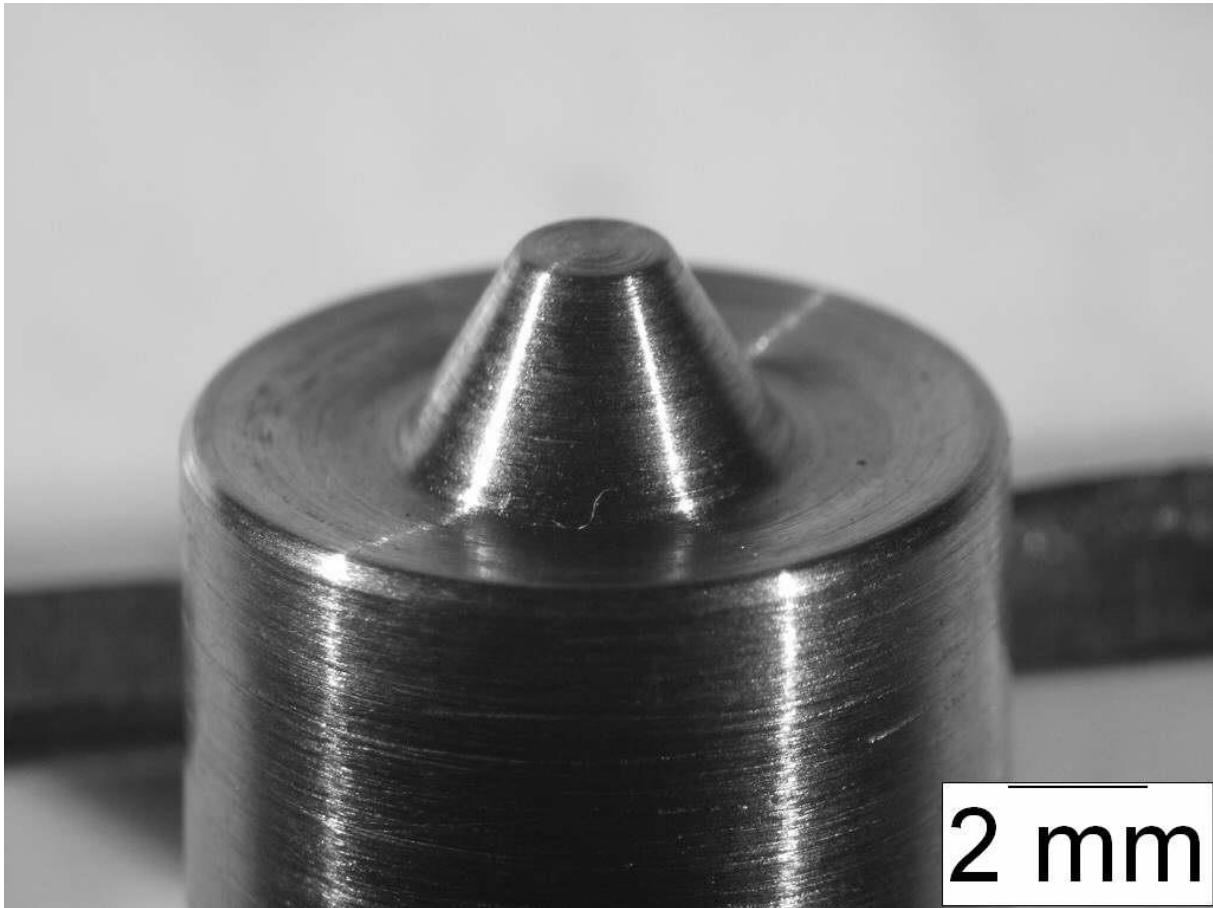
Figure 1 - Optical micrographs of different microstructures obtained by pre-heat treatments (a) initial material, (b) coarse lamellar, (c) fine lamellar, (d) duplex.

### B. FSW process

FSW joints were created at LORTEK Research Centre (Ordizia, Spain) using MTS ISTIR PDS FSW equipment in position control with (1) a tilt angle of  $2.5^\circ$  and (2) a position control strategy. The spindle of the welding machine was connected to a cooling system, in order to reduce its temperature by a water flow. A 20 l/min argon gas flow was also used to prevent oxidation of the welds. A W-25Re welding tool with a convex shoulder and conical pin was chosen (Figure 2). The shoulder diameter and the pin length were 12 mm and 2.8 mm respectively. 3 mm penetration was made in full matter for 120 mm transversally to the rolling direction of the plates. The plates were clamped to a stainless-steel backing plate. Calibration tests were initially performed to choose the optimal sets of parameters giving sound welds. During those tests, the experimental windows was limited to Welding Speed encompassed between 50 and 95 mm/min and Rotational Speed encompassed between 400 rpm and 460 rpm, outside of this window the weld were defective: we observe flash, tunnel defects, or no stir.

135

136 Numerous experiments were carried out, by varying the initial pre-heat treatment, of course, but also the welding  
137 speed and the rotational speed, to be sure that each initial pre-heat treatment would at least produce a defect-free  
138 weld. Table 3 summarises all the experiments carried out.



139

**Figure 2 - W-25Re welding tool.**

140

141

### **C. Design of experiments (DOE)**

142

143 In order to study the effect of welding and rotational speed of the tool, a design of experiments was set up. Table  
144 3 shows the L16 Taguchi table used for the experiments.

145 The results of the DOE were hardness along the weld and optical micrographs of the welds. Vickers hardness  
146 tests across the welds were carried out in a transversal section across all the zones (BM, TAZ, SZ, TAZ, and  
147 BM), 1 mm below the top surface of each weld. The testing conditions used were a load of 5 kg and a dwelling  
148 time of 10 s. The samples for microstructural observations were prepared by polishing with SiC abrasive papers.  
149 The polishing procedure started from very coarse P180 papers (200  $\mu\text{m}$  SiC particle diameter) to P4000 (5  $\mu\text{m}$   
150 SiC particle diameter). The final polishing was done with colloidal silica. Finally, the specimens were etched

151 with Kroll's reagent (2 ml HF + 5 ml HNO<sub>3</sub> + 100 ml H<sub>2</sub>O) for light optical microscope (OM) observations, or  
152 underwent electrolytic polishing (600 mL CH<sub>3</sub>OH + 360 mL C<sub>6</sub>H<sub>14</sub>O<sub>2</sub> + 60 mL HClO<sub>4</sub>, 30V, 5-10 s) for EBSD  
153 analysis.

154

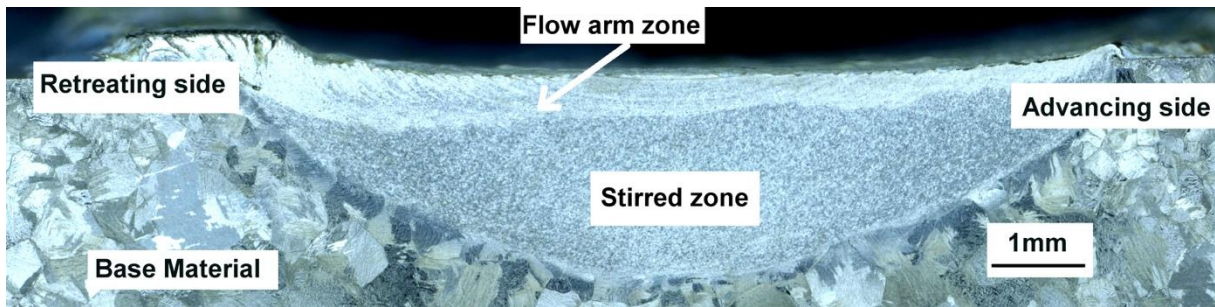
155

### 156 III. RESULTS AND DISCUSSION

#### 157 A. Microstructural analysis

158 The microstructural characterisation of sample no. 5 (coarse lamellar, speed 50 mm/min, rotation 420 rpm) is  
159 presented in Figure 3. One can clearly see that this FSW joint has no macroscopic defects such as porosity, lack  
160 of penetration, etc.

161



162

163 **Figure 3 - Cross-section perpendicular to the welding direction of a coarse lamellar sample welded at 50**  
164 **mm/min\*420 rpm.**

164

165

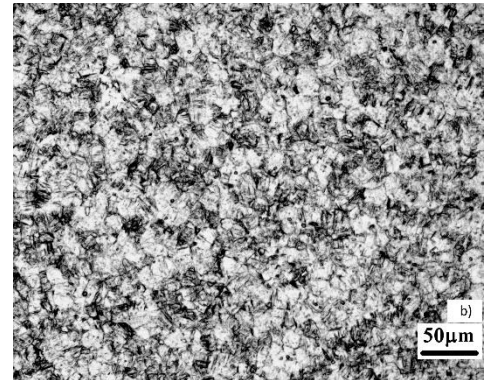
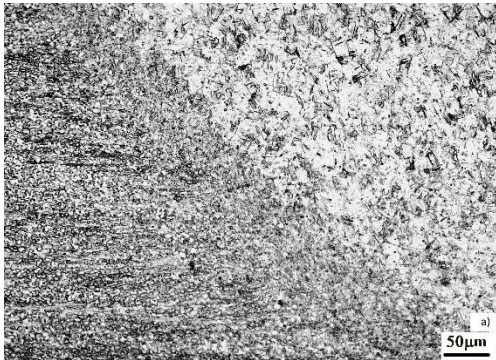
166

167 This sample shows a typical morphology for titanium alloy FSW joints. The base metal (BM), which is located  
168 far from the welded zone, undergoes no deformation or overheating. It therefore retains its original properties  
169 and microstructure. The heat affected zone (HAZ) undergoes heating without significant strain. The granular  
170 texture is identical to that of the base metal, but the dislocation population and the state of precipitation can  
171 change.

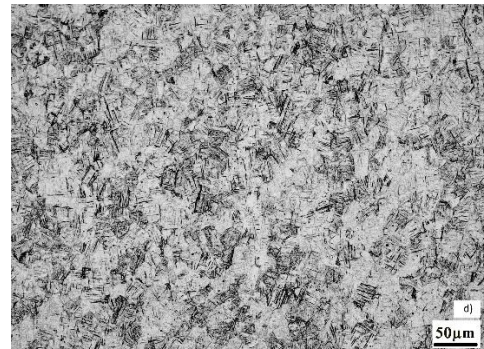
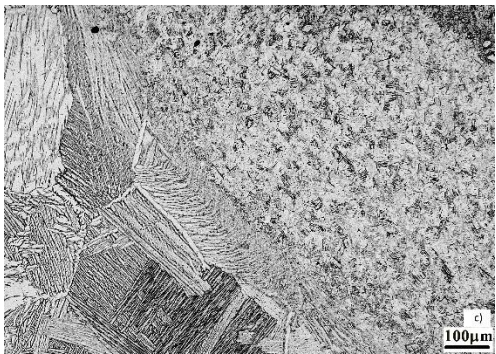
172 The thermo-mechanically affected zone (TMAZ) experiences both heating and plastic deformation during FSW,  
173 being characterised by a deformed structure brought about by the mechanical stirring of the tool. In the case of  
174 the present work, the TMAZ is limited to a very thin layer, due to the low thermal conductivity of titanium alloys  
175 and given that the pin is not threaded. The stirred zone (SZ), or nugget, undergoes the greatest plastic strain and  
176 temperature rise. The SZ is slightly larger than the pin.

177 Figure 4 shows the optical micrographs of the welding joints obtained with the four different initial  
178 microstructures. Each processing condition shows a similar microstructure in the SZ, which means that the  
179 changes occurring during the welding process are driven by the process itself. The initial heat-treatments have no  
180 significant effect on the microstructure of the welding zone.

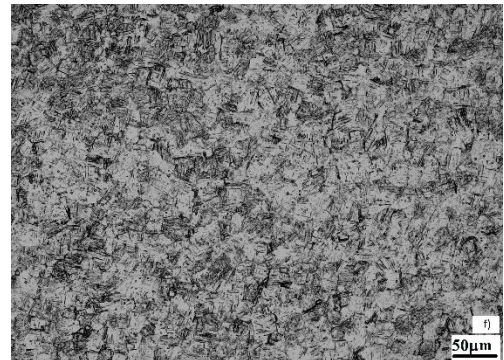
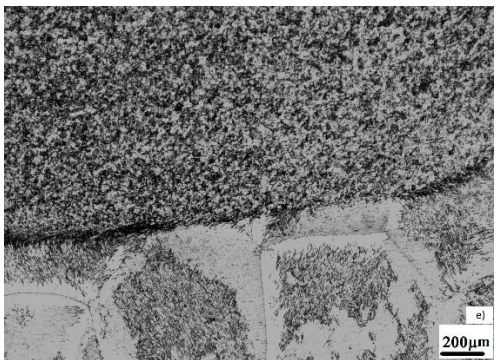
181



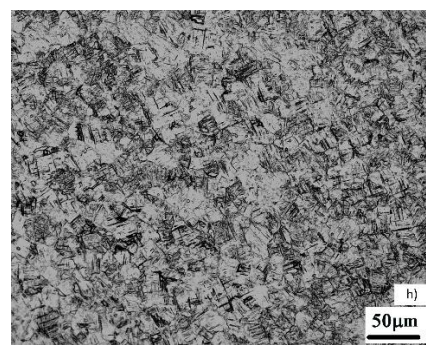
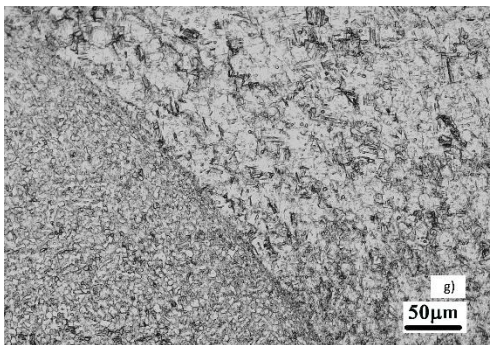
182



183

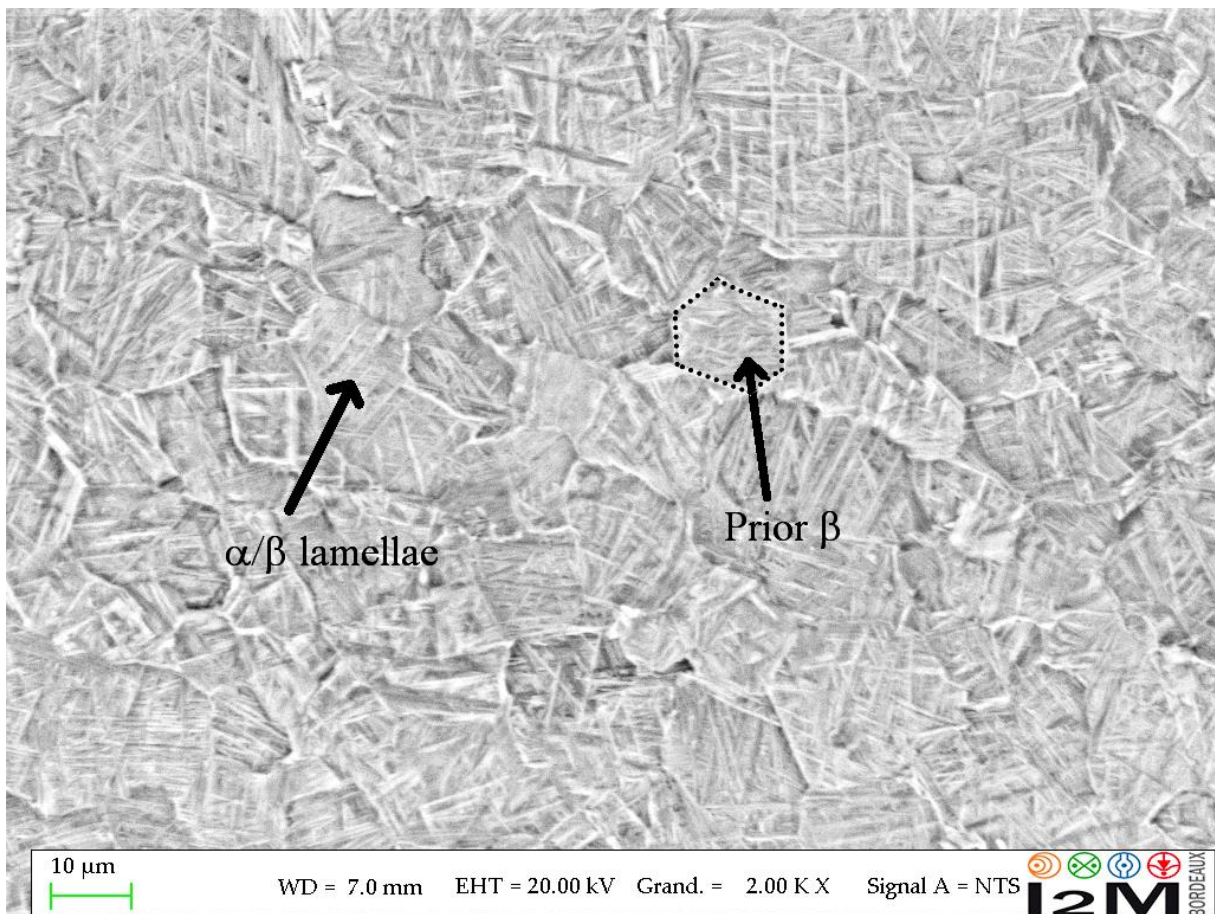


184



185 **Figure 4 - Optical micrographs: a) Initial microstructure: boundaries between SZ and BM (65 mm/min**  
186 **and 420 rpm), b) Initial microstructure: SZ (65 mm/min and 420 rpm), c) Coarse lamellar: boundaries**  
187 **between SZ and BM (50 mm/min and 420 rpm), d) Coarse lamellar: SZ (50 mm/min and 420 rpm), e) Fine**  
188 **lamellar: boundaries between SZ and BM (50 mm/min and 440 rpm), f) Fine lamellar: SZ (50 mm/min**  
189 **and 440 rpm), g) Duplex: boundaries between SZ and BM (50 mm/min and 460 rpm), h) Duplex: SZ (50**  
190 **mm/min and 460 rpm).**

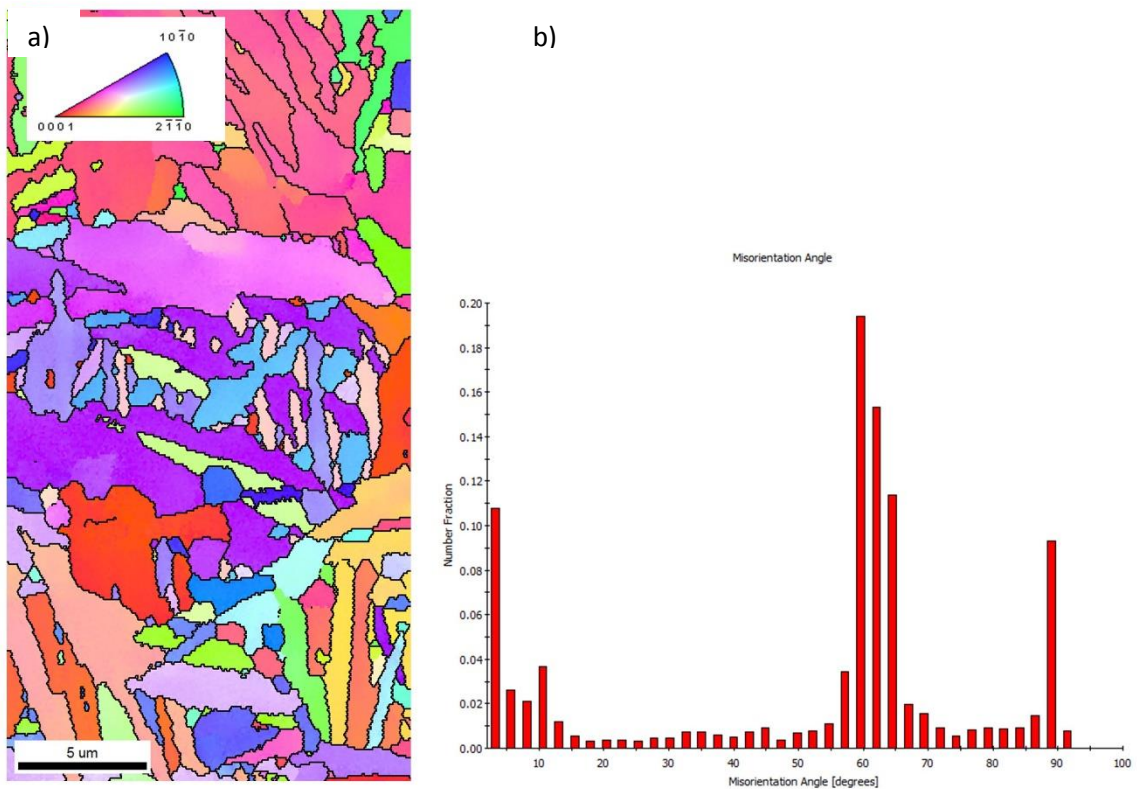
191  
192 Figure 5 shows a typical backscattered SEM image obtained in the SZ. Equiaxed cells composed of a fine  
193 intergranular Widmanstätten phase can be observed. The size of the cells (around 13-14  $\mu\text{m}$ ) is nearly the same,  
194 whatever the initial microstructure and welding conditions. The FSW processing produces a grain size reduction  
195 in the SZ for the large grains (grain size reduces from 735  $\mu\text{m}$  and 573  $\mu\text{m}$  to 13-14  $\mu\text{m}$ , for  $\beta$  annealed pre-  
196 treated samples), or an increase in grain size for the initial small grains (grain size increases from 6.5  $\mu\text{m}$  to 13-  
197 14  $\mu\text{m}$  for untreated and  $\alpha+\beta$  annealed pre-treated samples).



198 **Figure 5 - Backscattered SEM image in the SZ of the fine lamellar sample welded at 50 mm/min and 440**  
199 **rpm.**  
200

201

202 The fine intergranular Widmanstätten phase in the SZ is characterised by a fully  $\beta$  transformed structure ( $\alpha/\beta$   
203 lamellar structures). This suggests that (a) the peak temperatures in the SZ exceeded the  $\beta$  transus temperature  
204 during the process [29], and (b) the  $\beta \rightarrow \alpha + \beta$  phase transformation occurred during cooling for all types of welds,  
205 regardless of the initial heat treatment or process parameters.



206

207 **Figure 6 - OIM images of  $\alpha$  phase in the ZS of the fine equiaxed sample welded at 50 mm/min and 400**  
208 **rpm: (a) inverse pole figure map, (b) statistical misorientation angle distribution**

209

210

211 Figure 6 shows the microstructure obtained by the EBSD technique coupled with OIM equipment. An OIM scan  
212 was performed in the SZ centre for sample no. 1 (Table 3). The resolution of the SEM was too low to identify  
213 the very fine  $\beta$  phase, but the good indexation of the hexagonal close-packed  $\alpha$  phase revealed a typical basket-  
214 weave microstructure occurring during the  $\beta \rightarrow \alpha + \beta$  transformation. This indicates that the structure is not strain-  
215 hardened, which shows that this transformation occurs after the plastic deformation, that is to say during the  
216 cooling phase. The very thin alpha laths suggest that the cooling rate is quite high, similar to air quenching. The  
217 misorientation distribution of the  $\alpha$  grains shows a significant peak for the misorientation of  $60^\circ$ , which confirms

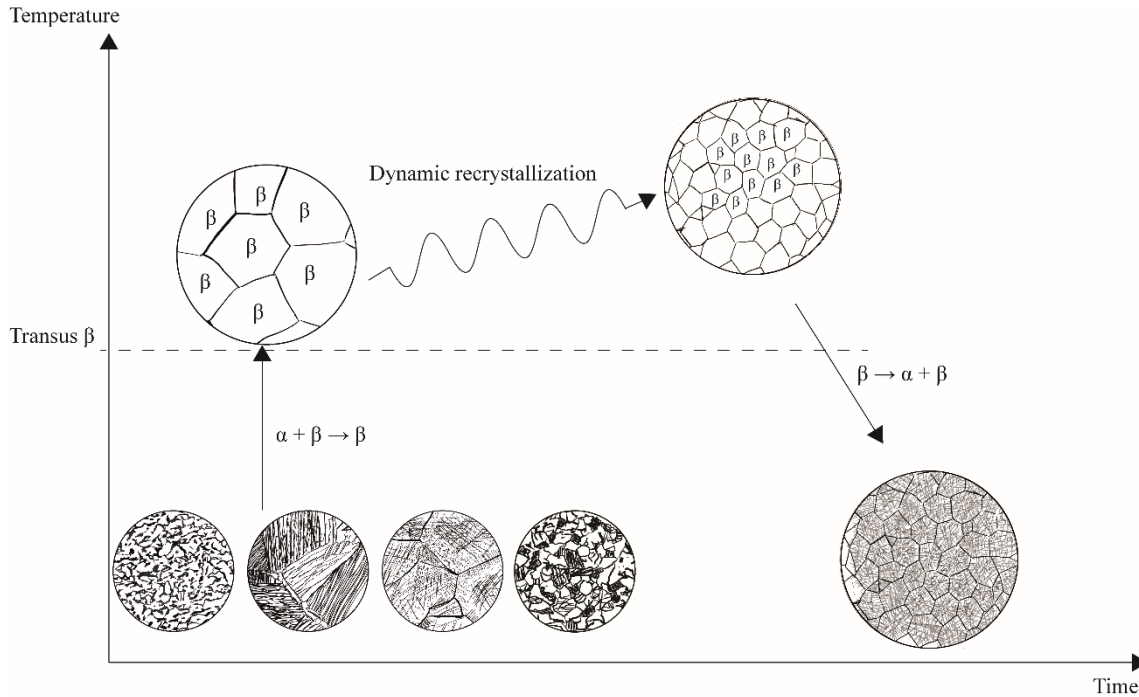
218 the  $\beta \rightarrow \alpha + \beta$  transformation, given that transformed  $\alpha$  and  $\beta$  phases satisfy the Burgers orientation relationship  
 219 defined by  $(110)_\beta // (0001)_\alpha$ ,  $[\bar{1}\bar{1}\bar{1}]_\beta // [2\bar{1}\bar{1}0]_\alpha$  and  $(\bar{1}12)_\beta // (01\bar{1}0)_\alpha$  [30,31].

220

221

**B. Genesis of microstructures**

222



223

224 **Figure 7 - Thermomechanical steps followed by the material during the FSW process**

225

226 Figure 7 shows the various thermomechanical steps followed by the material during the welding process.

227 First, the material undergoes a sudden rise in temperature, caused by (a) friction between the tool shoulder and  
 228 pin, and (b) plastic deformation. The resulting high temperature coupled with the plastic deformation tends to  
 229 promote a condition of dynamic recrystallization [32–34], which takes place usually at temperatures between 0.6  
 230 and 0.8 times the melting temperature  $T_m$ . For Ti-6Al-4V,  $T_m$  is about 1933 K, so that the DRX starting  
 231 temperature is about 1160 K, which is below the  $\beta$  transus (1268 K). Montheillet et al. [35] showed that the  
 232 “classical discontinuous“ dynamic recrystallization occurring by nucleation and growth of the new grains is not  
 233 observed in the  $\beta$  phase of the titanium alloy (due to the high rate of dynamic recovery associated with the large  
 234 stacking fault energy of the bcc structure). Instead, continuous dynamic recrystallization (CDRX) takes place,  
 235 i.e., grain fragmentation occurs by the generation of new grain boundaries [36]. This mechanism generates  
 236 reduced and equiaxed grains that could be much smaller than the initial one. R. Ding and al. [37] investigated

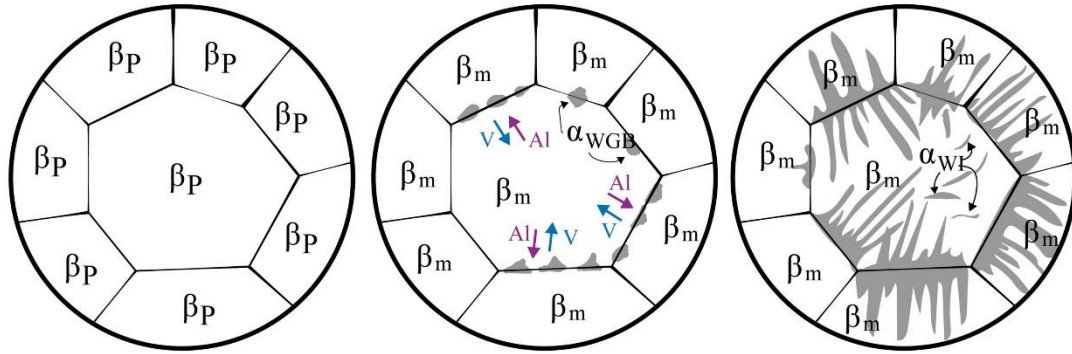
237 dynamic and/or metadynamic recrystallization when the Ti-6Al-4V alloy was processed in the  $\beta$ -phase field. The  
238 author obtained a similar recrystallized grain with embedded martensitic phase, as in Figure 6. In this paper, the  
239 recrystallized grain size stabilises at around 13-14  $\mu\text{m}$ , regardless of the initial heat treatment or process  
240 parameters, which suggests that the CDRX mechanism predominates with respect to  $\beta$  grain growth. It is known  
241 that  $\beta$  grain growth is rapid in the  $\beta$  phase field because of high temperatures and the absence of second-phase  
242 particles to impede grain boundary motion, but this phenomenon is totally masked in our case by the  
243 recrystallization phenomenon.

244

245 Afterwards, when the pin has moved away, heating by friction and by plastic power decreases drastically.  
246 Considering the low thermal conductivity of the Ti-6Al-4V alloy, it can be supposed that the material undergoes  
247 air quenching from the  $\beta$  phase field. In this case, during the rapid cooling, the  $\beta$  phase that is stable at high  
248 temperature will transform (at least partially) into a very fine intergranular lath phase. This transformation is  
249 similar to one occurring during the germination of an intergranular Widmanstätten phase (the same as one used  
250 for the fine lamellar heat treatment).

251 The  $\alpha$  phase precipitates preferentially at the prior  $\beta$  grain boundary. Colonies of  $\alpha_{\text{WGB}}$  lamellae then develop  
252 from this precipitation. Simultaneously, for fast cooling rates, a new  $\alpha_1$  phase develops in the matrix, forming  
253 sub-colonies. (Figure 8). The difference between the diffusion coefficients of the  $\alpha$ -stabiliser and  $\beta$ -stabiliser  
254 elements imposes growth of the platelet-shaped  $\alpha$  phase.

255 The air quenching undergone by the material is between 25 and 45°C/s approximately [38], but this is not  
256 enough to produce the  $\alpha'$  martensitic phase, which requires a cooling rate of  $> 160^\circ\text{C/s}$  [39].



$\beta_P$ :  $\beta$  prior

$\alpha_{WGB}$ :  $\alpha$  grain boundary

$\beta_m$ :  $\beta$  metastable

$\alpha_{WI}$ :  $\alpha$  intergranular

257

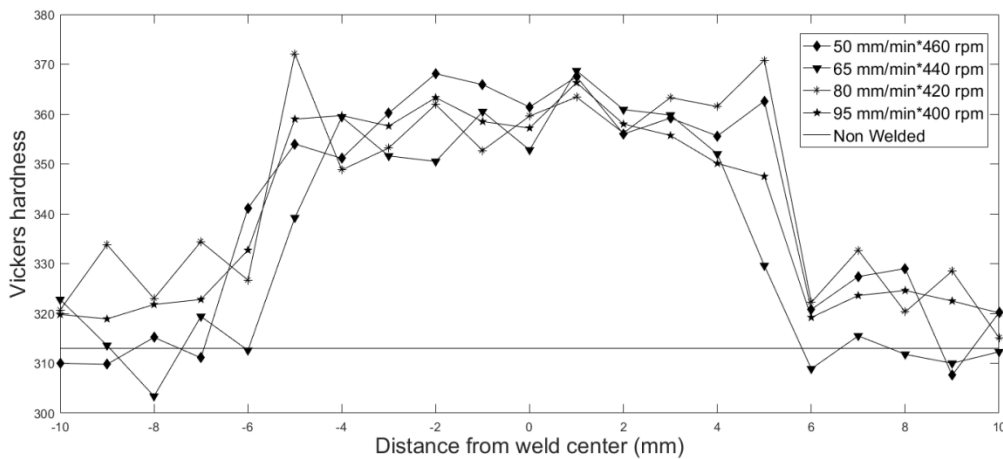
258

**Figure 8 -  $\beta \rightarrow \beta + \alpha$  Widmanstätten phase transformation**

259

260

**C. Vickers hardness profile**



261

262

**Figure 9 - Vickers Hardness profile across the weld for duplex base materials**

263

264 Typical Vickers hardness profiles across the welds are shown in Figure 9. The higher Vickers hardness is

265 observed in the stirred zone. The hardness in the base material is similar to that measured in non-welded

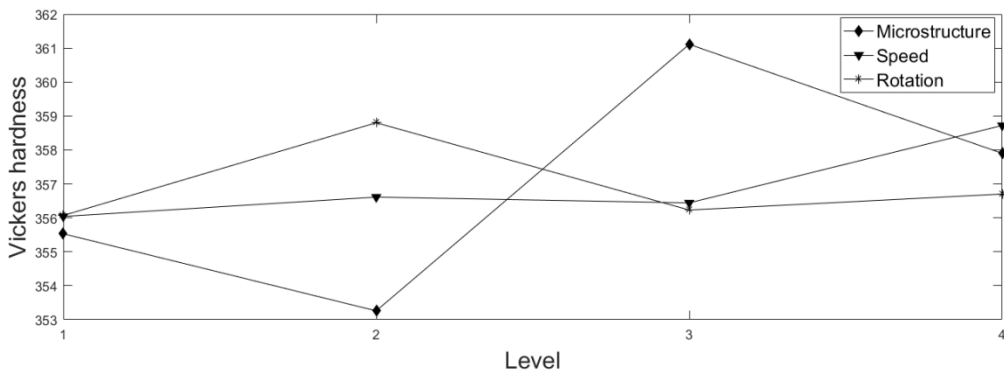
266 samples. It is commonly accepted that conventional physicochemical hardening (quenching) does not produce

267 any significant hardening for titanium and its alloys. The increase in hardness in the stirred zone can be  
 268 explained by the microstructure refinement in that zone according to the Hall-Petch relationship,

269 
$$H = H_0 + k_h \cdot d^{1/2}$$

270 where H is the hardness,  $H_0$  and  $K_h$ , two constants, and d, the grain size. The thin transition of hardness between  
 271 the SZ and the BM indicates that the HAZ is very thin, if not almost non-existent. The mean hardness in the SZ  
 272 (Table 3) is calculated by averaging the hardness of the nine central values around the centreline of the weld.  
 273 According to Table 3, the mean hardness is not sensitive to the welding process parameters, given the very small  
 274 difference (7.85 HV) between the highest and lowest values. According to other reports on FSW of Ti-6Al-4V  
 275 [23], this is due to the narrow window for rotational speed and welding speed values.

276 A simplified analysis of the variance was performed to give a clear picture of how far the process parameter  
 277 affects the response and the level of significance of the factor considered. The results of the Design of  
 278 experiments and the calculated response table for hardness are shown in Table 4 and Table 5 respectively. From  
 279 the main effects plotted in Figure 10, the optimal parametric combination for hardness optimisation is A3B4C2.  
 280 The ANOVA table for means is calculated and listed in Table 6. The F test is being carried out to study the  
 281 significance of the process parameters. The high F value indicates that the factor is highly significant in affecting  
 282 the response of the process. The ANOVA table for hardness shows that initial microstructure may have the  
 283 maximum effect on hardness while welding speed and rotation have less effect. Nevertheless, the response table  
 284 for hardness shows a very low variation for initial microstructure, proving that hardness in the stirred zone is not  
 285 sensitive to pre-heat treatment.



286  
 287  
 288 **Figure 10: Main Effects plot for Hardness**

289  
 290 **IV. CONCLUSION**

291

292 Several titanium joints, initially prepared with 4 different pre-heat treatments, were processed in FSW. Detailed  
293 microstructural analyses were performed in order to investigate the change in microstructure occurring during  
294 the process.

295 The main conclusions drawn from this study are as follows:

- 296 1) The FSW of Ti-6Al-4V produces a very thin TMAZ.  
297
- 298 2) During Friction Stir Welding of the Ti-6Al-4V alloy, the maximum temperature increase  
299 exceeds the  $\beta$ -transus temperature.  
300
- 301 3) The FSW processing produces a controlled and stable microstructure in the stirring zone,  
302 whatever the initial heat treatment or the welding conditions. This microstructure is  
303 characterised by a fully  $\beta$ -transformed structure in the form of lamellar  $\alpha/\beta$  structures, resulting  
304 from the  $\beta \rightarrow \alpha + \beta$  phase transformation. A typical basket-weave microstructure can be  
305 observed, with a  $60^\circ$  predominant misorientation. The thin  $\alpha$  laths are grouped within cells  
306 corresponding to the ex- $\beta$  grains present before the air quenching.  
307
- 308 4) The genesis of the microstructure can be divided into two steps. First, the plastic strain and the  
309 friction allow a sufficient temperature to be reached and plastic strain to achieve a continuous  
310 dynamic recrystallization (CRDX), which produces a stable  $\beta$  grain size of around 13-14  $\mu\text{m}$ .  
311 A reduction in grain size can be seen for large grains, corresponding to an initial heat-treatment  
312 above the  $\beta$  transus, and an increase in grain size can be seen for the initial small grains.  
313 Second, a fine  $\beta \rightarrow \beta + \alpha$  Widmanstätten phase transformation appears within the *ex-fully-*  
314 *recrystallized- $\beta$  grains*.  
315
- 316 5) Hardness in the stirred zone is not sensitive to pre-heat treatment.  
317  
318

### 319 **Acknowledgements**

320 This work was supported by IdEx Bordeaux within the framework of the Cross-border Joint Laboratory  
321 “Aquitania Euskadi Network In Green Manufacturing and Ecodesign” (LTC AENIGME). The authors gratefully

322 acknowledge Egoitz Aldemando (Ik4- LORTEK Research Centre, Ordizia, Spain) for carrying out the FSW  
323 joining.

324

## 325 REFERENCES

- 326 1. V.S. Godiganur, S. Biradar: *Int. J. Res. Eng. Technol.*, 2014, vol. 3, pp. 572–576.
- 327 2. C. He, Y. Liu, J. Dong, Q. Wang, D. Wagner, C. Bathias: *Int. J. Fatigue*, 2015, vol. 81, pp. 171–178.
- 328 3. P. Cavaliere, A. Squillace, F. Panella: *J. Mater. Process. Technol.*, 2008, vol. 200, pp. 364–372.
- 329 4. M.M.Z. Ahmed, S. Ataya, M.M. El-Sayed Seleman, H.R. Ammar: *J. Mater. Process. Technol.*, 2017, vol.  
330 242, pp. 77–91.
- 331 5. S.R. Kumar, V.S. Rao, R.V. Pranesh: *Procedia Mater. Sci.*, 2014, vol. 5, pp. 1726–1735.
- 332 6. M. Koilraj, V. Sundareswaran, S. Vijayan, S.R. Koteswara Rao: *Mater. Des.*, 2012, vol. 42, pp. 1–7.
- 333 7. A.H. Lotfi, S. Nourouzi: *Metall. Mater. Trans. A.*, 2014, vol. 45, pp. 2792–2807.
- 334 8. Y.S. Sato, S.H.C. Park, A. Matsunaga, A. Honda, H. Kokawa: *J. Mater. Sci.*, 2005, vol. 40, pp. 637–642.
- 335 9. J. Chen, R. Ueji, H. Fujii: *Mater. Des.*, 2015, vol. 76, pp. 181–189.
- 336 10. S.H.C. Park, Y.S. Sato, H. Kokawa: *Scr. Mater.*, 2003, vol. 49, pp. 161–166.
- 337 11. Y. Zhang, Y.S. Sato, H. Kokawa, S.H.C. Park: *Mater. Sci. Eng. A.*, 2008, vol. 488, pp. 25–30.
- 338 12. H. Fujii, Y. Sun, H. Kato, K. Nakata: *Mater. Sci. Eng. A.*, 2010, vol. 527, pp. 3386–3391.
- 339 13. P. Edwards, M. Ramulu: *J. Eng. Mater. Technol.*, 2010, vol. 132, 031006 (10 pages).
- 340 14. Y.N. Zhang, X. Cao, S. Larose, P. Wanjara: *Can. Metall. Q.*, 2012, vol. 51, pp. 250–261.
- 341 15. M.H. Shojaeefard, M. Akbari, A. Khalkhali, P. Asadi, A.H. Parivar: *Mater. Des.*, 2014, vol. 64, pp. 660–666.
- 342 16. Ş. Kasman: *Int. J. Adv. Manuf. Technol.*, 2013, vol. 68, pp. 795–804.
- 343 17. N.M. Daniolos, D.I. Pantelis: *Int. J. Adv. Manuf. Technol.*, 2017, vol. 88, pp. 2497–2505.
- 344 18. J. Wang, J. Su, R.S. Mishra, R. Xu, J.A. Baumann: *Wear.*, 2014, vol. 321, pp. 25–32.
- 345 19. A. Farias, G.F. Batalha, E.F. Prados, R. Magnabosco: *Wear.*, 2013, vol. 302, pp. 1327–1333.
- 346 20. L. Zhou, H.J. Liu, P. Liu, Q.W. Liu: *Scripta Mat.*, 2009, vol. 61, pp. 596–599.
- 347 21. H.J. Liu, L. Zhou, Q.W. Liu: *Mater. Des.*, 2010, vol. 31, pp. 1650–1655.
- 348 22. P. Edwards, M. Ramulu: *Sci. Technol. Weld. Join.*, 2010, vol. 15, pp. 468–472.
- 349 23. Y. Zhang, Y.S. Sato, H. Kokawa, S.H.C. Park, S. Hirano: *Mater. Sci. Eng. A.*, 2008, vol. 485, pp. 448–455.
- 350 24. S. Yoon, R. Ueji, H. Fujii: *Mater. Charact.*, 2015, vol. 106, pp. 352–358.
- 351 25. M. Esmaily, S. Nooshin Mortazavi, P. Todehfalah, M. Rashidi: *Mater. Des.*, 2013, vol. 47, pp. 143–150.
- 352 26. Y. Combres, C. Champin: *Tech. Ing.*, 1995, M1335. 33, pp. 24.

- 353 27. ASM International, ed., *Metallography and microstructures*, New ed, American Society for Metals, Metals  
354 Park, Ohio, 2004.
- 355 28. B. Hocheid, R. Klima, C. Beauvais, M. Rapin, C. Roux: *Mém Sci Rev Mét.*, 1970, vol. 72, pp. 583–590.
- 356 29. J. Su, J. Wang, R.S. Mishra, R. Xu, J.A. Baumann: *Mater. Sci. Eng. A.*, 2013, vol. 573, pp. 67–74.
- 357 30. M. Humbert, L. Germain, N. Gey, E. Boucard: *Acta Mater.*, 2015, vol. 82, pp. 137–144.
- 358 31. S.C. Wang, M. Aindow, M.J. Starink: *Acta Mater.*, 2003, vol. 51, pp. 2485–2503.
- 359 32. E. Ghasemi, A. Zarei-Hanzaki, E. Farabi, K. Tesař, A. Jäger, M. Rezaee: *J. Alloys Compd.*, 2017, vol. 695,  
360 pp. 1706–1718.
- 361 33. X.G. Fan, H. Yang, P.F. Gao, R. Zuo, P.H. Lei: *J. Mater. Process. Technol.*, 2016, vol. 234, pp. 290–299.
- 362 34. S. Lu, D. Ouyang, X. Cui, K. Wang: *Trans. Nonferrous Met. Soc. China.*, 2016, vol. 26, pp. 1003–1010.
- 363 35. F. Montheillet, L. Pallot, D. Piot: *7th Int. Conf. on Processing and Manufacturing of Advanced Materials,*  
364 *THERMEC 2011*, vol. 706-709, Quebec City, QC, 2012.
- 365 36. S. Gourdet, F. Montheillet: *Acta Mater.*, 2003, vol. 51, pp. 2685–2699.
- 366 37. R. Ding, Z.X. Guo, A. Wilson: *Mater. Sci. Eng. A.*, 2002, vol. 327, pp. 233–245.
- 367 38. A. Bardelcik, C.P. Salisbury, S. Winkler, M.A. Wells, M.J. Worswick: *Lightweight Struct.*, 2010, vol. 37, pp.  
368 694–702.
- 369 39. F. Le Maitre: *Revue de Métallurgie*, 1970, vol.67, pp. 563.

370 **FIGURE CAPTIONS**

371 Figure 1 - Optical micrographs of different microstructures obtained by pre-heat treatments (a) initial material,  
372 (b) coarse lamellar, (c) fine lamellar, (d) duplex

373 Figure 2 - W-25Re welding tool

374 Figure 3 - Cross-section perpendicular to the welding direction of a coarse lamellar sample welded at 50  
375 mm/min\*420 rpm.

376 Figure 4 - Optical micrographs

377 (a) Initial microstructure: boundaries between SZ and BM (65 mm/min and 420 rpm)

378 (b) Initial microstructure: SZ (65 mm/min and 420 rpm)

379 (c) Coarse lamellar: boundaries between SZ and BM (50 mm/min and 420 rpm)

380 (d) Coarse lamellar: SZ (50 mm/min and 420 rpm)

381 (e) Fine lamellar: boundaries between SZ and BM (50 mm/min and 440 rpm)

382 (f) Fine lamellar: SZ (50 mm/min and 440 rpm)

383 (g) Duplex: boundaries between SZ and BM (50 mm/min and 460 rpm)

384 (h) Duplex: SZ (50 mm/min and 460 rpm)

385 Figure 5 - Backscattered SEM image in the SZ of the fine lamellar sample welded at 50 mm/min and 440 rpm

386 Figure 6 - OIM images of  $\alpha$  phase in the ZS of the fine equiaxed sample welded at 50 mm/min and 400 rpm: (a)  
387 inverse pole figure map, (b) statistical misorientation angle distribution

388 Figure 7 - Thermomechanical steps followed by the material during the FSW process

389 Figure 8 -  $\beta \rightarrow \beta + \alpha$  Widmanstätten phase transformation

390 Figure 9 - Vickers Hardness profile across the weld for duplex base materials

391